Chapter 2
A Subject-Specific Framework to Inform Musculoskeletal Modeling: Outcomes from the IUPS Physiome Project

J. Fernandez, P. Hunter, V. Shim, and K. Mithraratne

Abstract The International Union of Physiological Sciences (IUPS) Physiome Project was established as a framework for creation, sharing and dissemination of multiscale mathematical models of human physiology. We present a suite of subject-specific musculoskeletal models that were developed using this framework. This process starts with subject-specific geometry development using high-order cubic Hermite elements suitable for describing the topology of complex musculoskeletal structures accurately. These geometries are able to be customized using free-form deformation techniques with data from Computed Tomography (CT), Magnetic Resonance Imaging (MRI) or anthropometric information derived from motion capture. We describe how the deformations of soft tissues are referred to a microstructural curvilinear coordinate system. The constitutive laws that describe the stress-strain behavior of soft tissue are also referred to this anatomically based material coordinate system. Finally, we highlight the finite deformation mechanics framework through a set of clinically relevant examples. These examples include the efficient creation of a subject's hip model from CT for implant testing with validation; customization of bone and muscle geometry; a hybrid free-form deformation and mechanics method for assessing gait; coupled blood flow and solid deformation of the lower limb to examine the influence of deep vein thrombosis and patellofemoral joint contact pressure following a vastus release and tibial medialization.

We also examine the recent focus on multiscale approaches and how this integrates with subject-specific musculoskeletal modeling. The Physiome Project is a computational framework for understanding human physiology by integrating computational models at all levels of biological organization. Recent developments in multiscale modeling have made use of the markup languages, ontologies, databases and software tools, developed as part of the Physiome Project. Using these markup languages, including AnatML, FieldML and CellML, we are able to take unique subject-specific information at the whole organ level, which informs micro level

J. Fernandez (✉) · P. Hunter · V. Shim · K. Mithraratne
Auckland Bioengineering Institute, The University of Auckland, 70 Symonds Street, Auckland 1010, New Zealand
e-mail: j.fernandez@auckland.ac.nz

B. Calvo, E. Peña (eds.), *Patient-Specific Computational Modeling*, Lecture Notes in Computational Vision and Biomechanics 5,
DOI 10.1007/978-94-007-4552-0_2,

models and in turn initiates cell level remodeling. The cell level information is then passed up the model hierarchy to inform change in micro level architecture and modification of material behavior at the macro level. We illustrate this multiscale approach by presenting a model of the knee joint to explore a possible pathway to osteoarthritis. This is initiated by abnormal loads at the whole knee coupled with a micro model of the cartilage-bone interface, which is linked to both cartilage and bone cell remodeling.

2.1 Challenges in Modeling

The challenges faced in subject-specific modeling are similar in all organ systems. In this chapter we focus on musculoskeletal modeling, which has strong links with orthopedics and physiotherapy where patient-based treatment is increasingly being sought in clinical practice. Some of these modeling challenges include: (i) how to model the anatomy and tissue structure efficiently and in a 'patient-specific' manner; (ii) how to define constitutive laws (stress-strain behavior) that capture experimentally observed mechanical behavior and are not over-parameterized; (iii) how to link the constitutive parameters to underlying tissue micro-structure such as the unique fiber distributions within different muscles and within individuals; (iv) how to couple the equations of large deformation mechanics to the equations representing other physical processes such as blood flow in the lower limb; (v) and how to link the spatial scales to inform tissue level behavior from cell processes such as active muscle contraction and tissue remodeling, which is specific to different disease states, age groups and can account for 'patient-specific' treatments. Figure 2.1 depicts the modeling approach adopted in this chapter whereby a subset of geometries is derived from a database; microstructural information such as fiber fields are described within soft tissues; geometries are customized to individual profiles; macro level solid mechanics analysis is performed; solid stress from various activities is coupled to fluid flows; and the macro level solutions are used as boundary conditions for micro level models.

2.2 Geometry Development

One goal of the IUPS Physiome project (Hunter, 2004) was to develop a database of anatomically-based geometries as the first step in computational mechanics. Figure 2.2 shows how this database was developed from a number of sources including an anatomical skeleton model (SOMSO, www.somso.de), scanned using a Polhemus laser scanner and the soft tissues digitized from the Visible Man (VM) (Ackerman, 1998). The Somso skeleton allowed for accurate depiction of the complex joint articular surfaces at the end of the bones and attachment points, while the VM high resolution images provided information about the detailed three-dimensional relationships between muscles, tendons, ligaments and other organs.

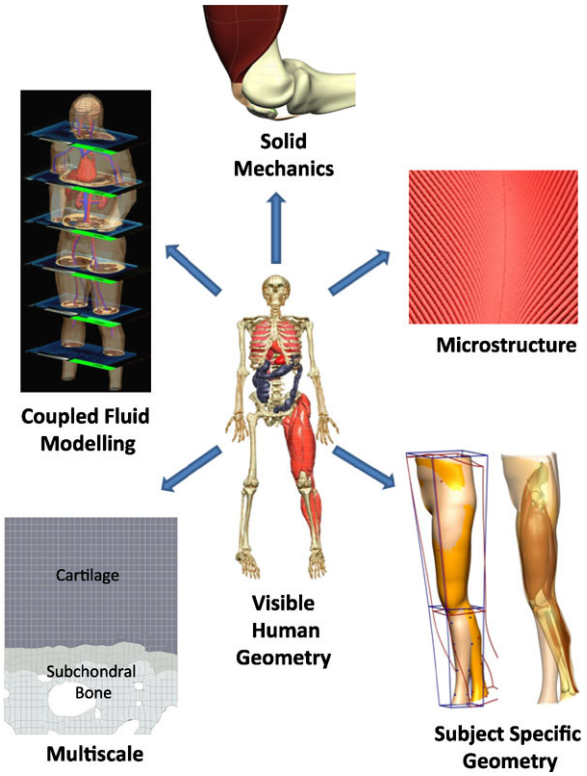

Fig. 2.1 Modeling framework used to simulate the musculoskeletal system. A database of generic geometries is developed from the Visible Human dataset; free-form deformation methods are used to customize the models using subject-specific data; microstructural material information is obtained from imaging and experiment; solid mechanics simulations predict spatial stress and strain in response to physiologically-based boundary conditions; whole organ models are mapped to micro mechanics using multiscale methods; and embedded vessel networks coupled to solid mechanics are used to predict fluid flows

These were collected in a supine reference pose as this was the position the data were imaged. Over the last 10 years additional images have been collected from the Visible Female (Spitzer et al., 1995) which is sliced at every 0.33 mm (as opposed to 1 mm for the VM) providing greater detail around the knee joint region where structures like the menisci and cartilage are typically a few millimeters thick. Additional imaging modalities have also been used including Magnetic Resonance Imaging (MRI) and Computed Tomography (CT) to add to the growing collection of data. The additional modalities offer further benefits by allowing customization of generic models and validation of model mechanics by comparison with Tagged MRI, dynamic X-ray (fluoroscopy) and dynamic ultrasound. The geometries are being collected into hierarchical modeling ontologies (Hunter and Borg, 2003) to facilitate data exchange among scientists contributing to the Physiome Project. The collected datasets utilize AnatML (www.physiome.org.nz/anatml_viewer), a markup language describing the linkages between the different structures using definitions from Grey's anatomy (Gray, 2008) and Anatomica (FCAT, 2011).

Once the raw segmented data is acquired, a set of 3D parameterized FE meshes suitable for mechanics are developed. The three-dimensional FE meshes have basis (or shape) functions determined from the tensor product of 1D interpolation func-

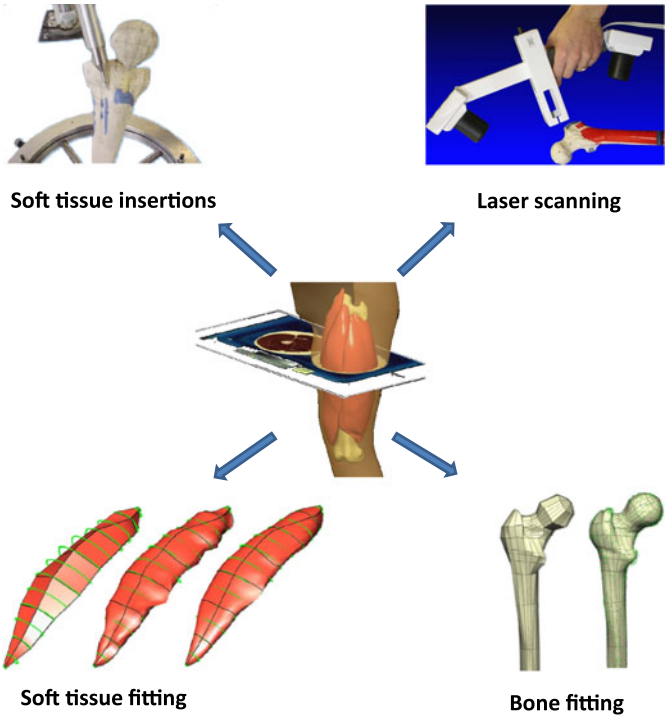

Fig. 2.2 A subset of the lower limb model derived from the Visible Man dataset with bone geometry and soft tissue insertions from a physical Somso model. The process of fitting the rectus femoris (quadriceps) muscle and femur (thigh) bone to data is illustrated

tions. These four 1D cubic Hermite basis functions are given by

$$\begin{aligned} \Psi_1^0(\xi) &= 1 - 3\xi^2 + 2\xi^3; \qquad \Psi_2^0(\xi) = \xi^2(3 - 2\xi); \\ \Psi_1^1(\xi) &= \xi(\xi - 1)^2; \qquad \Psi_2^1(\xi) = \xi^2(\xi - 1), \end{aligned} \tag{2.1}$$

where ξ is the normalized local or element coordinate which is defined from 0 to 1. These cubic Hermite elements differ from the usual Lagrange family finite elements in that they preserve both the continuity of the nodal values (C^0 continuity), and their first derivatives (C^1 continuity). This provides many advantages in constructing a finite element geometry, particularly of biological structures such as muscles and other organs that typically have smooth surfaces (Wriggers et al., 2001). Moreover, the realistic geometries are useful in such applications as virtual surgery and medical education. Another attractive feature of cubic Hermite elements is that fewer numbers of elements are required for complex geometries. C^1-continuous interpolation also provides a smooth change in the surface normal across element boundaries and this provides numerical benefits when solving contact mechanics problem. Interpolation of the spatial coordinates of line elements in space with cu-

bic Hermite basis functions is given by

$$u(\xi) = \Psi_1^0(\xi)u_1 + \Psi_2^0(\xi)u_2 + \Psi_1^1(\xi).\frac{du}{ds}\bigg|_1 L + \Psi_2^1(\xi).\frac{du}{ds}\bigg|_2 L, \tag{2.2}$$

where u is x, y or z if the field is geometry and du/ds is the derivative of the spatial coordinate with respect to a measure of distance, chosen to be arc-length here. Subscripts 1 and 2 refer to node numbers and superscripts 0 and 1 are the zeroth and first derivatives, respectively. L is the physical arc length along the curve. To ensure we have continuity with respect to arc-length we enforce the condition that the magnitude of du/ds should be 1. The interpolation can be any field in general such as stress, temperature or fiber information and more details can be found in Fernandez et al. (2004).

Now that we have established the element primitive we fit the elements to segmented data using a least-squares fitting procedure. We employ a face fitting routine for surfaces of the volume mesh and define a face objective function, $F(u_n)$, consisting of two components, namely the data error and a smoothing constraint given by

$$F(u_n) = \sum_{d=1}^{N} w_d \left\| u(\xi_{1d}, \xi_{2d}) - z_d \right\|^2 + F_s(u_n), \tag{2.3}$$

where the data error is the summation of the square of the distances between each data point, z_d, and its orthogonal projection $u(\xi_{1d}, \xi_{2d})$ on the relevant face. Each point can be weighted based on importance using w_d. The smoothing constraint, $F_s(u_n)$, is appended to the objective function as a penalty function defined by

$$\begin{aligned} F_s(u_n) = \int_0^1 \int_0^1 \Bigg\{ & \alpha_1 \left\| \frac{\partial u}{\partial \xi_1} \right\|^2 + \alpha_2 \left\| \frac{\partial u}{\partial \xi_2} \right\|^2 + \alpha_3 \left\| \frac{\partial^2 u}{\partial \xi_1^2} \right\|^2 + \alpha_4 \left\| \frac{\partial^2 u}{\partial \xi_2^2} \right\|^2 \\ & + \alpha_5 \left\| \frac{\partial^2 u}{\partial \xi_1 \partial \xi_2} \right\|^2 \Bigg\} d\xi_1 d\xi_2, \end{aligned} \tag{2.4}$$

which is the second order Sobolev norm (Bradley et al., 1997) used as the smoothing constraint to account for sparse and scattered data. Constants α_i $(i = 1, \ldots, 5)$ are the Sobolev weights (penalty parameters) and each term has a distinct effect on the final shape of the fitted object. The first two terms (α_1, α_2) control the arc-length, while the third and fourth terms (α_3, α_4) control the arc-curvature in the ξ_1 and ξ_2 directions, respectively. The last term (α_5) represents the face area. For instance, if the weight associated with the cross-derivative term is set to a relatively higher value, one might end up with a smaller face area. All Sobolev weights must be at least an order lower than the weight associated with the data error component, w_d, which is usually taken as 1.0.

We highlight two examples of model fitting depicted in Fig. 2.2. If the data set is sparse, such as shown with the rectus femoris muscle (one of the quadriceps) and if the Sobolev weights are all set to have minimal effect then the fitting will produce an

oscillatory shape in the muscle. This is an artifact arising from the data being dense in the radial direction but sparse in the longitudinal direction. If, however, we place more weight on the curvature in the longitudinal direction and increase smoothing on the face area we arrive at a more anatomically correct shape. This shows that the Sobolev weights can account for incomplete or non-uniform data sets. In the second example we have a bone to fit (the femur) with a uniform and dense cloud of data from a scanned source. There is usually less need to increase Sobolev smoothing parameters in such a case as the data is sufficient and homogeneously distributed for an accurate fit. However, if we want to place more emphasis on a particular region such as the greater and lesser trochanters then we can increase the data point weights for those features. The fitting algorithm will then ensure a better fit in those regions.

2.3 Combining Sparse Data Sets

Situations may arise when only a limited amount of geometric data is available, such as when the knee is imaged using MRI but we want a whole limb model. Another situation, which may limit data availability, is when excessive imaging is undesirable such as when ionizing radiation from CT is involved. Subject specific finite element models require a complete dataset and therefore a new method of supplementing patient CT images with images from the Visible Human CT was developed (Shim et al., 2007). This method uses the previously described cubic Hermite elements and least squares fitting procedures. Figure 2.3 outlines the method starting with dividing the patient CT and Visible Human CT into the same number of anatomically defined regions. Second, within each region we transformed slices from the Visible Human CT slice to the patient CT slice using landmarks at the beginning and end of each region. Third, we selected a minimal number of slices within each region of the Visible Human CT to transform and fill the gaps in the patient CT set. It was found that with only 12 CT slices we were able to generate smooth and accurate meshes of the proximal femur with a geometric root mean square (RMS) error of less than 1 mm and peak errors less than 8 mm. We tested this method on three patient data sets, generating FE meshes of the pelvis using only 10 CT slices with an overall RMS error less than 3 mm. Considering that linear meshes usually require about 70–100 pelvic CT slices (in axial mode) to generate FE models, our method has brought a significant data reduction to the automatic mesh generation step.

Using this technique we validated the resulting finite element model developed from hybrid CT data with mechanical experiments (Shim et al., 2008) as shown in Fig. 2.4. Three cadaveric embalmed pelvises were strain gauged and FE models were generated from the CT scans. Material properties for cancellous bone were obtained from the CT scans and assigned to the FE mesh using a spatially varying field embedded inside the mesh while the mechanical characteristics of other materials used in the model were obtained from the literature. For each pelvis, five different

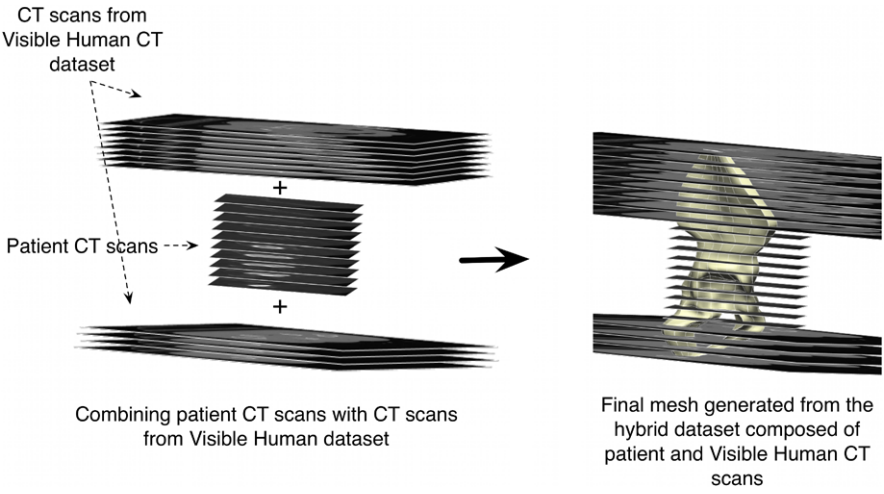

Fig. 2.3 A finite element mesh of the pelvis developed from a hybrid CT dataset comprising both patient and visible human data

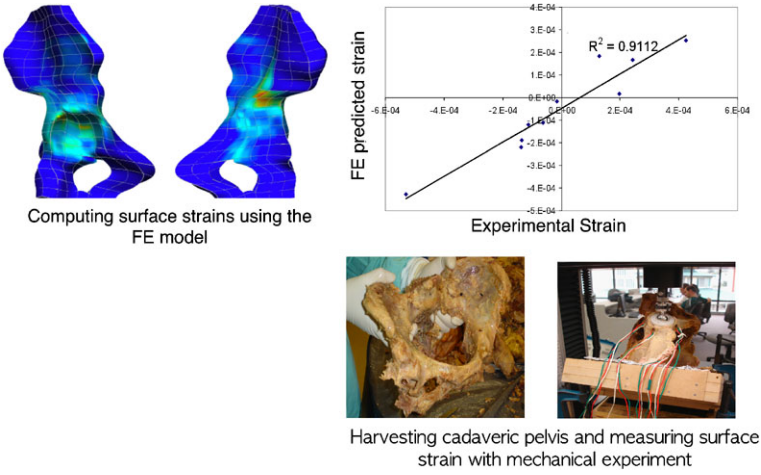

Fig. 2.4 Experimental setup of the pelvic validation trial for the hybrid finite element model. Shown are the FE surface strains, mechanical rig and comparison between experimental and predicted strain

FE meshes with a varying number of patient CT slices (8–12) were generated to determine how many patient CT slices were needed for good accuracy. All five mesh types showed good agreement between the model and experimental strains with an R^2 of 0.9. Meshes generated with incomplete data sets showed very similar stress distributions to those obtained from the FE mesh generated with complete data sets.

2.4 Subject-Specific Customization

A database of geometries is extremely useful for sharing and disseminating models amongst the scientific community, especially using the popular Visible Human dataset. They can be used to study population-based mechanics primarily in healthy individuals. However, when studying diseased joints, pathology leading to deformed geometry (such as cerebral palsy) or for focused studies aimed at predicting the outcomes of intervention a subject-specific geometry is required. The original database of geometries serves as a good basis to morph and fit to patient data obtained from MRI, CT or motion capture. We utilize a technique, based on free-form, to rapidly morph complex geometries using only a few control points (Fernandez et al., 2005).

The "host-mesh" fitting method described below is a free-form deformation technique used to perform geometric transformations consisting of both Euclidean (translation and rotation) and Affine (Euclidean plus scaling and shearing) operations on arbitrary parameterized meshes. The structure of the host mesh is a parallelepiped in these examples, but can in general be any shape. The size of the host mesh is determined from experience, however, as a general rule it should be close to the size of the object being deformed and the number of degrees freedom of the host mesh depends on the control the user wishes to have over the deformation and object anatomy. The object being morphed is embedded within the host and when the host is morphed the object within it also undergoes the same transformation. For most cases one to three-element host meshes will suffice to provide enough degrees of freedom to control its deformation. We demonstrate this method in a couple of scenarios shown in Fig. 2.5 including changing the articular features of femoral bone, changing the attachments of ligaments and morphing the rectus femoris muscle.

The host-mesh technique permits morphing of anatomical geometries given a limited number of data points. This is most useful where only a limited data set is available, such as a partial MRI or CT, or only discrete measures can be obtained (such as motion capture). The quality of fit can be controlled through weighting the data points (placing more weight on important regions) or through constraining the host that the body lies within. A useful illustration is the femur, which is known to vary between patients and is influenced by gender (with females having a wider quadriceps angle) and pathology (such as children with cerebral palsy with highly curved femurs). When performing finite element analyses the resulting stress distribution is influenced by the geometric profile and so obtaining a quick fit is desirable when performing large population studies. In this case 24 landmark points were identified from a CT-scanned femur but could also be obtained from other modalities. Each data point represents a distinct extremity such as a peak or groove in the bone. The host was divided into 3 segments (elements) for separate control of the shaft, proximal and distal ends. Greater freedom was allowed for the femur ends while the shaft, which had limited data available, was allowed only to radially expand, twist and lengthen. The blue markers indicate the landmark points and the red markers show their desired final positions. The undeformed host (blue) was distorted to the red host in order to minimize the distance between the blue and red markers in a weighted least squares sense. The fitting procedure used to distort

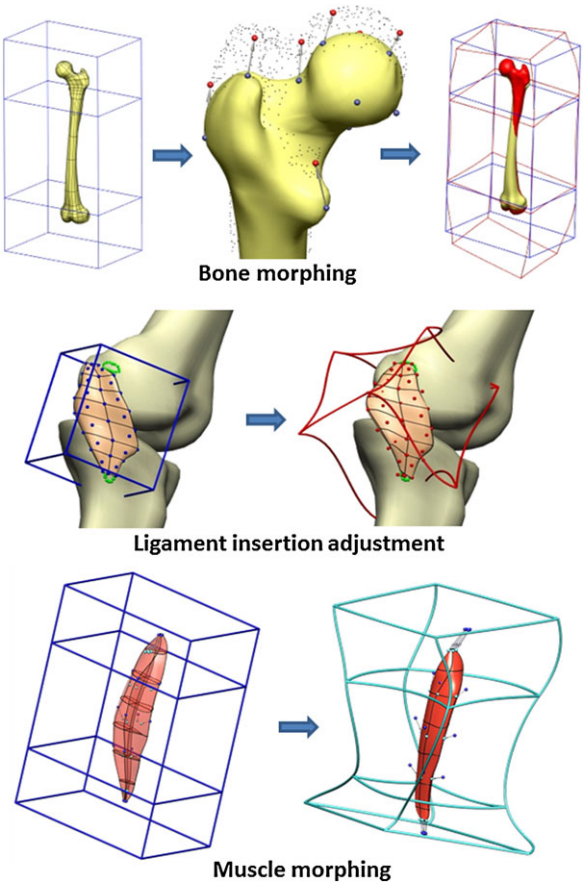

Fig. 2.5 Host-mesh customization of the femur (*top*), medial collateral ligament insertion (*middle*) and rectus femoris muscle (*bottom*)

the mesh in order to minimize the data error is identical to that described in (2.3) and (2.4) for fitting.

The host mesh can also be used to adjust small features while maintaining the remaining geometric shape. Ligament attachments vary between patients, as observed in MRI, and can be modified due to surgery to correct pathology. Illustrated in Fig. 2.5 is a new ligament attachment specified by green markers on the femur. The medial collateral ligament was morphed so as to match the insertion into the femur while maintaining the original ligament origin at the tibia. In this example only a sparse set of data existed (the insertion points), so we increased the Sobolev smoothing to assist the fit by placing weights on the host-mesh curvature. This ensured that the new ligament was not distorted.

Soft tissues can come in a variety of deformed poses and shape depending on the orientation the subject is imaged. While muscles typically have textbook profiles defined based on cadaveric studies it may be useful to rapidly customize a generic muscle to another subject. Here we have chosen an extreme example whereby the generic rectus femoris muscle (one of the quadriceps) derived from the Visible Male

is customized to a subset of points taken from the Visible Female dataset. Muscle size is useful because it affects the force generation capacity in computation. We identified a set of landmarks at the ends of the muscle and radially along the length of the axis (a total of 20 points). The same sites were located on the female muscle set using Visible Female images and we performed the fit to minimize the distance between the marker sets. The resulting mesh closely resembled the female muscle and to check we performed a least squares fit against the fully segmented female muscle giving an RMS of less than 3 mm.

2.5 Mechanics

Once we have the desired geometry we aim to predict the finite deformation given a material property description and boundary conditions (Nash and Hunter, 2000). Modeling mechanics is presented in the context of the patellar joint, which is further elaborated in Sect. 2.8 with applications. Figure 2.6 shows the first step, which is to identify the muscle shapes and fiber orientations in the quadriceps. This may be done using Diffusion Tensor Imaging or Ultrasound. For this work we participated in a complete cadaver dissection to learn about muscle anatomy, ligament and tendon insertions and surface fiber orientations. The muscles were photographed and a mapping of surface fiber orientation was extruded through the muscle volume. This was fitted as finite element field information and is shown for the rectus femoris muscle (with bi-pennation angle).This was repeated for all the quadriceps and hamstring muscles. This process draws on the fitting procedures described in Sect. 2.2.

Second, we solved for soft tissue deformation due to muscle contraction in the complete patellar complex. The virtual work statement for the problem at hand in the absence of body forces can be written as

$$\int_{V_0} \frac{1}{J} T^{\alpha\beta} F^j_\beta \frac{\partial \delta u_j}{\partial \upsilon_\alpha} dV_0 = \int_{S_c} f_c \delta u^c_j dS_c, \tag{2.5}$$

since the muscles were undergoing large deformation (greater than 10 % strain). V_0 is the undeformed volume and S_c is the surface in contact used to account for the interaction between muscles and between the patella cartilage and femoral condyles. δu_j is the virtual displacement, δu^c_j is the variation of the contact gap and $F^j_\beta = \partial x_j / \partial \upsilon_\beta$ is the deformation gradient tensor which maps between the deformed spatial coordinates x_j, and material coordinates, υ_β. The Jacobian, J, is the determinant of the deformation gradient tensor, F and f_c is the frictionless contact force, which is implemented using a penalty based method with the complete details described in Fernandez and Hunter (2005). $T^{\alpha\beta}$ is the 2nd Piola-Kirchoff stress tensor,

$$T^{\alpha\beta} = \frac{\partial W}{\partial E_{\alpha\beta}} + p a^{\alpha\beta}_\upsilon + T_0 \delta^\alpha_1 \delta^\beta_1, \tag{2.6}$$

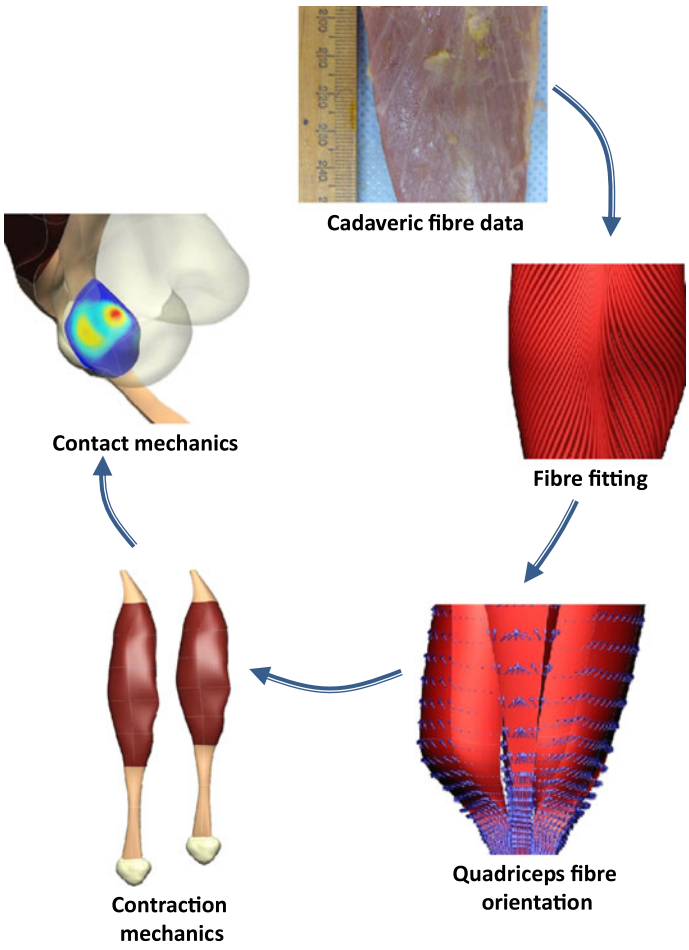

Fig. 2.6 Mechanics framework for the patellofemoral joint starting with a representation of fiber information from a cadaver, which is described as a field within a finite element mesh and repeated for the full set of quadriceps muscles. A muscle contraction is simulated, which shortens the muscle and pulls on the patella and the resulting patellar cartilage contact stress is predicted

and defined with respect to the undeformed curvilinear material coordinate system, υ_α. W is a strain energy density function and $E_{\alpha\beta}$ are the Green-Lagrange strain components. The hydrostatic pressure, p, arises in order to satisfy volume conservation and T_0 is the second Piola Kirchoff equivalent of the Cauchy active stress (muscle contraction). The contravariant metric tensor $a_\upsilon^{\alpha\beta} = \partial\upsilon_\alpha/\partial x_k.\ \partial\upsilon_\beta/\partial x_k$ is the inverse of the right Cauchy deformation tensor (covariant metric tensor).

We have used a number of constitutive laws depending on the availability of experimental data and modeling assumptions. A 'St-Venant Kirchoff' strain energy density function, a particular case of hyperelastic materials for a homogeneous isotropic material, was used for bone and cartilage, and for tendon we

adopted a transversely isotropic version of the well-known Mooney Rivlen material (Rivlin, 1948) with information derived from the literature. With muscle, however, we have available a number of instruments to perform muscle experiments and so have adopted a micro-structurally based constitutive law, the 'pole-zero' law (Hunter, 1995) for passive muscle,

$$W = k_{\alpha\beta} \frac{E_{\alpha\beta}^2}{|a_{\alpha\beta} - E_{\alpha\beta}|^{b_{\alpha\beta}}}, \tag{2.7}$$

where W is a strain energy density function, $E_{\alpha\beta}$ are Green's strain components referred to a microstructural fiber axis, $a_{\alpha\beta}$ are the strain limits (poles) and $k_{\alpha\beta}$, $b_{\alpha\beta}$ are the scaling and curvature control parameters, respectively.

Those models that include some form of active muscle behavior have been based on one of three approaches: (i) rheological models based upon Hill-type relationships (Hill, 1938) and have been shown to be more reliable in predicting forces and comparing with experiments; (ii) models employing physiological reasoning and 'cross-bridge' kinetics via Huxley-based models (Huxley, 1957); (iii) the final group is a recent addition and links the macro and micro scales by having low-order variable models of the whole muscle via approximations of the 'cross-bridge' theory maintaining biophysically meaningful variables. Examples include the 'distribution moment' model by Zahalak (2000) and the HMT model of Hunter et al. (1998). Here we used the model of Hunter and add a contractile force in the fiber direction to simulate muscle action given by

$$\sigma_0(\lambda, \mathrm{Ca}_{actn}) = \frac{(\mathrm{Ca}_{actn}.[\mathrm{Ca}^{2+}]_{\max})^h}{(\mathrm{Ca}_{actn}.[\mathrm{Ca}^{2+}]_{\max})^h + (c_{50})^h} \sigma_{ref}\big[1 + \beta(\lambda - 1)\big], \tag{2.8}$$

where σ_0 is the active tension added to the fiber direction and given by the calcium-tension derived from the 'fading-memory' model, which is based on the hill type model (Hunter, 1995). Ca_{actn} is the level of activation (non-dimensional calcium value), λ is the sarcomere stretch length, $[\mathrm{Ca}^{2+}]_{\max}$ is the intracellular calcium concentration for maximum activation, c_{50} is the concentration at which isometric tension is 50 % of its maximum, h is the hill coefficient, T_{ref} is the active isometric tension when $\lambda = 1$ and β is the slope parameter.

The model was driven by a combination of patellofemoral kinematics (derived from motion capture) and simulated muscle contraction, which shortens the muscle and pulls on the patella via the tendon resulting in patellar cartilage contact stress. The model was solved as a series of quasi-static steps.

2.6 Coupling Mechanics and Free-Form Deformation

The free-form deformation (FFD) technique (host-mesh fitting) is a useful tool for customization and rapidly transforming body shapes into different poses. This has the benefit of being able to compute muscle length change given only kinematics

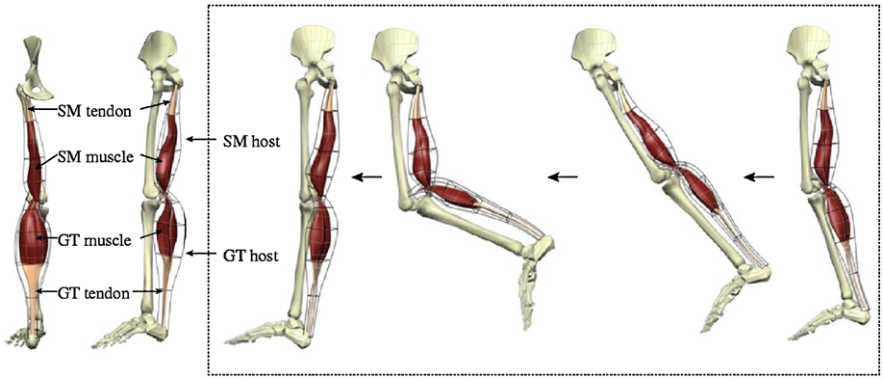

Fig. 2.7 Hybrid host-mesh mechanics of the semimembranosus and semitendinosus muscles during gait

from sources such as motion capture and X-ray fluoroscopy. However, while efficient it does not take into account the wrapping of muscle around bones and other muscles, or the different lengthening of tendon and muscle due to material stiffness. We have coupled the original FFD method with the mechanics framework previously established to solve mechanics on a coarse representation of a muscle (a host-mesh), which in turn passes on this deformation to the detailed muscle inside (Fernandez et al., 2005). In this way different regions of the muscle will undergo varying degrees of deformation providing physiologically accurate shapes. If the host mesh is close to the actual embedded muscle then the volume of the muscle is also preserved. More importantly, the muscles inside will interact with other surrounding tissues and so account for sliding between muscles and with bone.

The deformed lower limb bones and stance of cerebral palsy (CP) children fully utilize the subject-specific customization tools as the new bone shapes are substantially different in profile to a healthy generic model. First, we customize the geometry to the patient including the complete muscle bundle. Figure 2.7 highlights the technique for the hamstrings (semimembranosus, semitendinosus) and the gastrocnemius as these muscles are typically lengthened by surgeons and cross the knee joint. We then collect motion capture data from both a healthy control and CP patient. A host mesh similar in shape and size is placed around each muscle and material properties are assigned based on the location of tendon and the muscle belly. Computed kinematics are used to drive the model and change the location of the muscle attachment points. A mechanics deformation problem consisting of relatively fewer degrees of freedom is solved using displacement based boundary conditions while ensuring that the embedded muscles do not penetrate one another. In a subsequent step the shape of the embedded muscle is updated and the new muscle lengths are computed.

The host-mesh can also make reasonable predictions of muscle lengths and shape changes using purely geometric constraints (Oberhofer et al., 2009). This offers attractive benefits to those in the animation industry where efficient methods of morphing characters to anatomically-correct poses may assist artists. Figure 2.8 shows

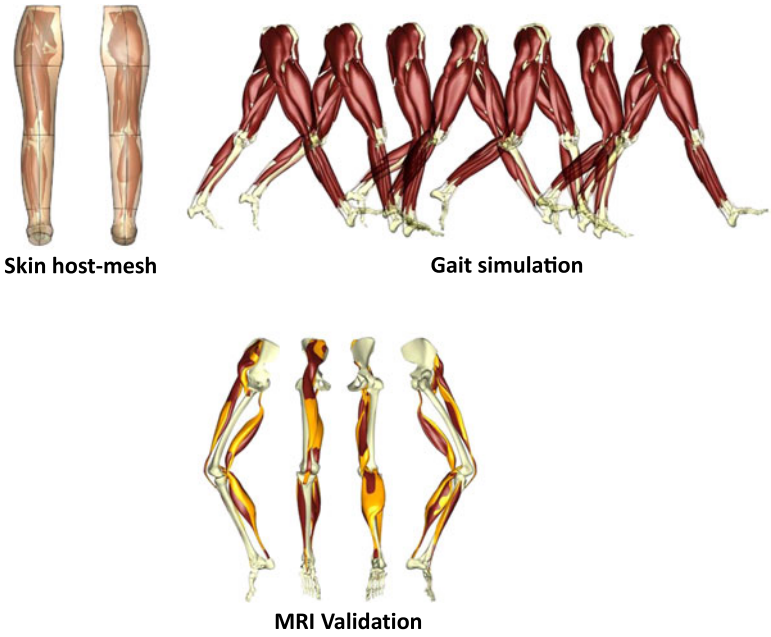

Fig. 2.8 Skin host-mesh fitting used to deform the complete lower limb muscle set (*red muscles*) during gait and validation against MRI derived muscles (*yellow muscles*)

a skin-shaped host mesh used to accurately deform 20 muscles of the lower limb by using information from the surrounding skin. In this case the host mesh was taken to be the volume defined by the actual skin, as opposed to the simpler shapes previously used, and the muscles were embedded within. Deformation driven by motion capture data produced a realistic walking simulation and we evaluated the shape changes of 5 muscles by comparing the predicted deformations with magnetic resonance image data in two lower limb positions (15° and 45° flexion). The predicted muscle positions shown in red were compared with MRI derived muscle shapes (shown in yellow) producing an average RMS error of 3.7 mm, which shows an excellent fit for muscle shapes predicted without mechanics.

2.7 Evaluating Compression in Deep Vein Thrombosis

Deep vein thrombosis (DVT), which is characterized by the formation of thrombi in deep veins, is a well-known problem following long haul flights (economy class syndrome) or extended hospital stays. The common factor is prolonged immobility and it is associated with other complications including chronic venous insufficiency and pulmonary embolism. The three main thrombogenic factors are stasis, hypercoagulability and injury to the vessel wall with the main treatments being either medicinal

(anticoagulents) or mechanical (static or intermittent compression). We shall examine static compression due to its low cost and popularity among air travelers using this technique through compressive stockings. Despite its use the effect of compression is not fully understood. It is believed to cause reduction in deep vessel cross-section area, which in turn results in increased flow velocities. Another hypothesis is that shear stress and cyclic strain can influence cellular mechanisms to dissolve fibrin and prevent thrombus formation. A number of studies (Downie et al., 2007, 2008) have looked at modeling external compression and resulting blood flow in deep veins. All these models, however, have either employed images (e.g. MRI) directly (Dai et al., 1999; Downie et al., 2007, 2008; Narracott et al., 2007) or used the deformation of 2D continuum models (plane strain analysis) of surrounding soft tissue structures to reconstruct the deformed (collapsed) geometry of vessels. The computational model presented here is a 3D soft tissue continuum model undergoing large deformations (finite elasticity) due to applied external compression with a 1D flow network of major deep vessels embedded within the 3D continuum. Coupling between fluid and soft tissue is achieved via the vessel wall constitutive equation that describes the relationship between vessel radius and the transmural pressure. The latter is the difference between the fluid pressure and soft tissue hydrostatic pressure which arises due to the incompressibility of the soft tissue material.

The solid mechanics framework previously described is now extended to include a coupled one-dimensional blood flow network. The patient-specific geometry of both the soft tissue continuum and vein network is anatomically based and was developed using data derived from magnetic resonance images (MRI) using the fitting techniques previously described. The soft tissue includes all the muscles, subcutaneous fat layers and skin. The combined tissue mass was treated as an incompressible hyperelastic material with homogeneous isotropic properties. The mechanical characteristics of the tissue was described using a quadratic Mooney-Rivlin constitutive model with the coefficients $C_{10} = C_{20} = 10$ kPa (Meier and Blickhan, 2000). The computational flow model was the 1D Navier-Stokes equation comprising continuity and momentum relations given by

$$\frac{\partial R}{\partial t} + V\frac{\partial R}{\partial x} + \frac{R}{2}.\frac{\partial V}{\partial x} = 0 \quad \text{and} \tag{2.9}$$

$$\frac{\partial V}{\partial t} + (2\alpha - 1)V\frac{\partial V}{\partial x} + 2(\alpha - 1)\frac{V^2}{R}.\frac{\partial R}{\partial x} + \frac{1}{\rho_f}\frac{\partial P}{\partial x} + \left(\frac{2\nu\alpha}{\alpha - 1}\right)\frac{V}{R^2} = 0, \tag{2.10}$$

where R is the radius of the vessel, V is the mean velocity and P is the fluid pressure. ρ_f and ν are fluid density and kinematic viscosity respectively. α is the velocity profile parameter and the velocity profile is given by

$$u = \left(\frac{\gamma + 2}{\gamma}\right).V.\left[1 - \left(\frac{r}{R}\right)^{\gamma}\right] \quad \text{and} \quad \gamma = \frac{2 - \alpha}{\alpha - 1}. \tag{2.11}$$

The constitutive equation of the vein wall which describes the mechanical characteristics (vessel radius–transmural pressure relationship) was defined

as a cubic polynomial of radius ratio R/R_0 by fitting the experimental data (Dobrin et al., 1988) obtained from a canine femoral vein,

$$P_{tr} = (P - p) = a\left(\frac{R}{R_0}\right)^3 + b\left(\frac{R}{R_0}\right)^2 + c\left(\frac{R}{R_0}\right), \tag{2.12}$$

where P_{tr} is the transmural pressure (difference between fluid and hydrostatic pressures), R_0 is the uncollapsed (reference) radius and a, b and c are the polynomial fitting coefficients.

Once compression is applied, the transmural pressure is computed as the difference between the fluid and soft tissue hydrostatic pressure. The latter arises due to the incompressibility of the soft tissue material. Transient flow governing equations are solved using the McCormack finite difference method (Anderson, 1995). The vascular network geometry was reconstructed with respect to the deformed soft tissue continuum to examine the degree of reduction in vessel cross-section area caused by gross deformation of the tissue continuum (without taking the hydrostatic pressure effects into account).

Simulation results from the computational model show a reasonably good agreement with the results reported in the literature on the degree of deformation in vein cross-section area estimated using MRI (Downie et al., 2008). The mean radius change of the venous network due to the gross deformation was found be insignificant (less than 2 %). The hydrostatic pressure distribution in response to the application of external compression is depicted in Fig. 2.9. The distribution of hydrostatic pressure was obtained by fitting it as a tri-linear FE field. The fitted hydrostatic pressure field was then interpolated to determine the external pressure acting on the vessel wall at each finite difference grid point of the venous flow network. The reduction in cross-section area at 1.0 ml/s based on a MRI study (Narracott et al., 2007) has been reported to be about 62 ± 10 %. The predicted value from this study compares reasonably well with the experimental data. Simulations also showed that increase in mean flow velocity due to compression resulted in increased wall shear stress (WSS), which stimulates endothelial cell activation and influences the release of tissue plasminogen activator (t-PA), which then converts plasminogen to active plasmin which dissolves fibrin and prevents thrombus formation.

2.8 Mechanics of the Patella

The patellar is a component of the knee that focuses the quadriceps muscles onto the tibia to enable the extensor action of the knee. Despite its role as a pivot to increase the moment arm (increasing the efficiency of the quadriceps) relatively less attention has been focused on its mechanics compared to the tibiofemoral joint. We have used the above framework to create the first fully 3D patellar integrated into a 3D continuum of muscles, tendons and ligaments to investigate the influence on joint loading from the action of muscle contraction (Fernandez and Hunter, 2005). Such a model has the potential to inform non-invasive treatment strategies on a patient basis

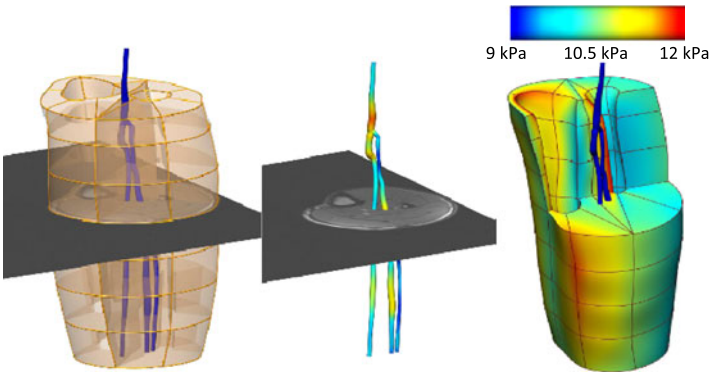

Fig. 2.9 Fitted 1D cubic FE mesh of the flow network embedded within 3D soft tissue (*left*); Radius field (cubic Hermite) in the flow network (*middle*); and hydrostatic pressure distribution of the calf at deformed state (*right*) [scale: 9 kPa (*blue*)–12 kPa (*red*)]

or predict the possible outcomes of surgery intervention such as a vastus lateralis release.

Figure 2.10 shows a knee joint from a healthy subject's MR data including muscles, ligaments, cartilage and bones. A generic model of the soft tissue was customized to the MR data and the bone was further divided into cortical and cancellous bone. Material properties were assigned to the bone regions using a grid point method independent of the mesh resolution using the 'St Venant Kirchoff' constitutive law. The fiber distribution was derived from a cadaveric study whereby the surfaces of fibers were taken from images and projected on the muscles. This has recently been extended by including fiber direction estimates using Diffusion Tensor Imaging sequences in an MRI. The motion of the tibia was derived from motion capture experiments and the patellar movement was controlled by the tension in the patellar ligament, contraction of the muscle tissues and contact with the femoral condyles. The model predicted the contact force, surface cartilage pressure and patellar kinematics in response to a healthy loading. Specifically, for normal gait we got two distinct regions of contact at contralateral toe-off (the highest loading point during gait) with a large contact area on the lateral facet and a small contact region on the medial facet. The peak in red represents 10 MPa.

We simulated two orthopedic procedures recommended for the alleviation of patellofemoral pain, the vastus lateralis (VL) release and the medialization of the tibial tubercle (as part of a Maquet procedure). The VL release works by excising a small region of muscle that inserts into the lateral portion of the patellar. Given the lateral facet is the most loaded (with the largest face) it is most often associated with osteoarthritis. The load on the lateral side is now reduced, which is exhibited by a medial shift in the cartilage contact pressure map. The original pressure distribution showed two distinct contact regions (with a peak on the lateral side). This has now migrated towards the middle and the two sites of contact have merged to form a single central contact patch. Patellar kinematics was relatively unchanged except for a slight increase in medial tilt.

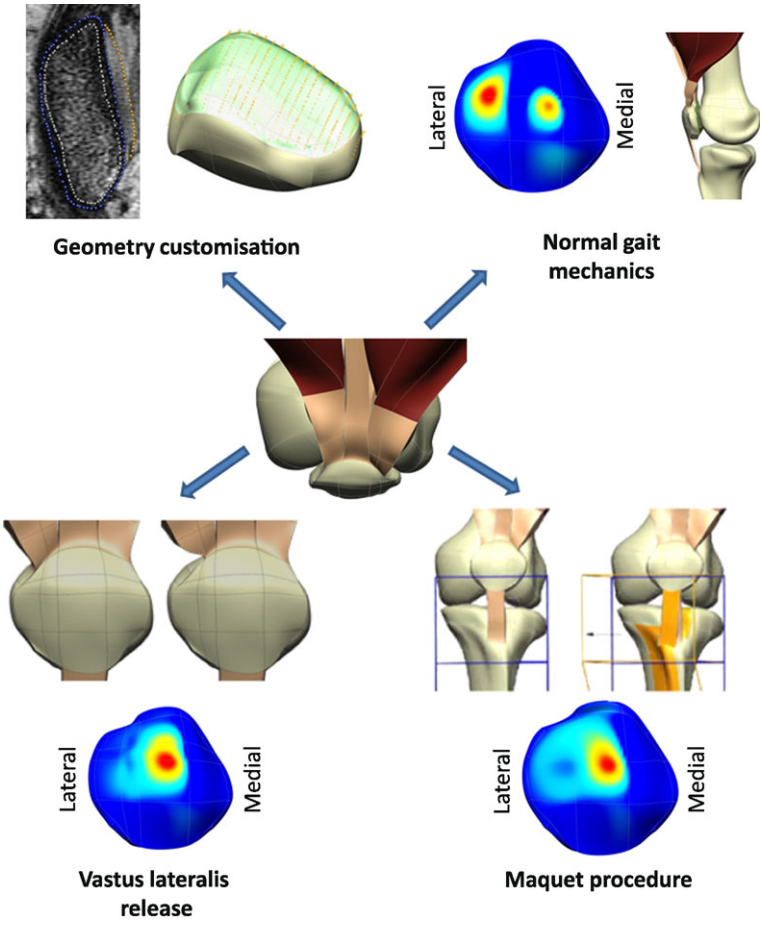

Fig. 2.10 Patient-specific customization of patella containing accurate topological descriptions of cancellous bone, cortical bone and articular cartilage; simulation of healthy gait showing contact pressure at contralateral toe-off; simulating a vastus lateralis release producing significant medial migration in patellar contact; and Maquet procedure predicting minor medial shift in patellar contact

Next we investigated medialization of the patellar tendon attachment point (part of the Maquet procedure) and used the host-mesh technique to morph the patella tendon insertion site (the tibial tuberosity) medially. In this case the contact pattern also migrated medially but some contact still remained on the lateral side. Patellar kinematics showed an increase in medial translation and medial tilt. The two simulations show that the Maquet procedure, which is generally more invasive, is more subtle in the contact redistribution but leads to more altered kinematics. In contrast, the VL release can be performed via key hole surgery (less invasive) has a subtle effect on kinematics but is better at completely alleviating loading from the lateral facet by directly affecting the muscle force.

2.9 Coupled Bone Cartilage Mechanics

The initiation of osteoarthritis has been linked to the onset and progression of pathologic mechanisms at the cartilage-bone interface. In order to evaluate this process we have developed a multiscale model using the open-source ontologies developed for the Physiome Project with cartilage and bone descriptions at the cellular, micro and macro levels. In this way we can effectively model the influence of whole body loadings at the macro level, the influence of bone organization and architecture at the micro level and have cell level processes determine bone and cartilage remodeling. Cell information is then passed up the spatial scales to modify micro architecture and provide a macro spatial characterization of cartilage inflammation. Figure 2.11 shows this framework being used to explore a common link with a widely reported knee injury (Anterior Cruciate Ligament Deficiency—ACDL) to proinflammatory mediators as a possible pathway to initiate osteoarthritis.

To simulate remodeling we designated the healthy strain state (normal gait) as homeostatic equilibrium, where bone and cartilage are maintained and no remodeling occurs. We then simulated the altered cartilage strains due to loading from ACLD. The difference between the homeostatic and ACLD strains was the excitation for bone remodeling to initiate. Micro models of cartilage (seen as red cubes in Fig. 2.11) are spatially placed across the bone cartilage interface to capture an average strain in that 1 mm^3 region. For each micro model, the average strain was then applied to the surface of the detailed micro bone-cartilage model and we modeled the propagation through the cartilage, zone of calcified cartilage (ZCC) and subchondral bone regions. The micro model was repeatedly run with each simulation representing a week's worth of loading. After each simulation the geometry was remodeled (through calling a cell level model) and the simulations were conducted again with the new bone architecture producing new strain patterns in both the bone, ZCC and cartilage. For both the macro and micro models, the bones and cartilage were treated as deformable linear elastic materials with the Young's modulus and Poisson's ratios for cartilage ($E = 10$ MPa, $\nu = 0.46$), ZCC ($E = 100$ MPa, $\nu = 0.3$) and bone ($E = 1$ GPa, $\nu = 0.3$). The micro FE model had a depth of 450 μm for cartilage, 200 μm for the zone of calcified cartilage (ZCC) and 350 μm for subchondral bone.

The micro model was informed by the parameters obtained from two cell models. A bone remodeling algorithm (Pivonka et al., 2008) based on the RANK-RANKL-OPG pathway, which predicts the number of active osteoblasts (to deposit bone) and osteoclasts (to absorb bone) implemented in CellML (Garny et al., 2008). The cell model used micro strains as excitation to predict temporal concentrations of osteoblasts and osteoclasts over their life cycle, from precursor cells to active working cells and finally apoptosis (cell death). The osteocyte sensors are strategically placed at numerical integration points within each element and inform the FE nodes excitation signal used to drive remodeling. Each node then calls the CellML bone model to determine the osteoblast/osteoclast numbers to provide the rate of remodeling, which is directioned normal to each surface. Similarly, a cartilage damage prediction model was developed based on the work of Nam et al. (2009), which quantitatively describes the action of nuclear factor-kappa B (NF-κB) signaling cascade

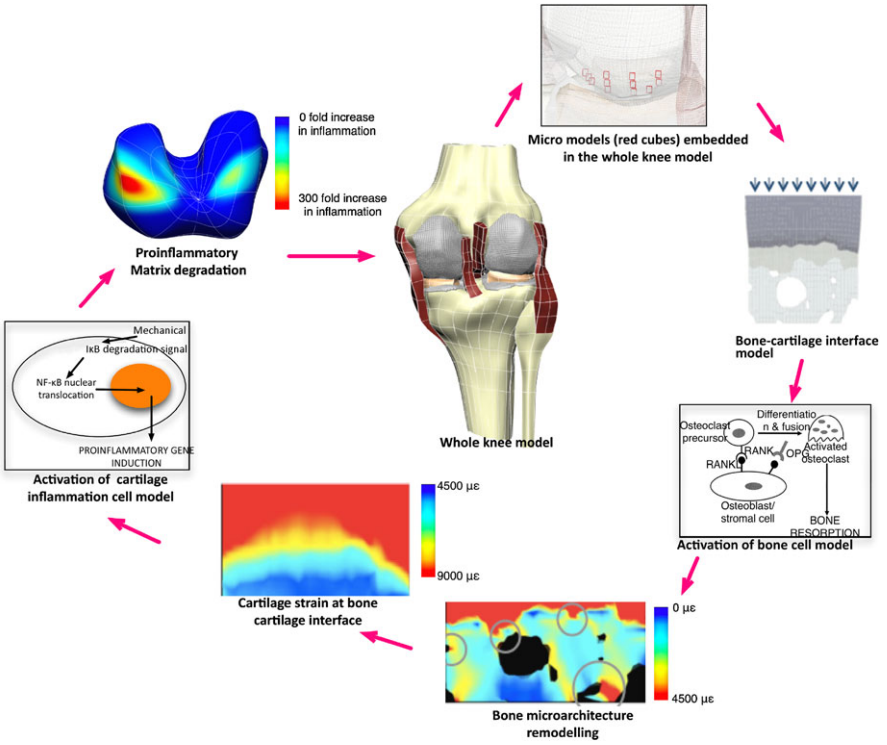

Fig. 2.11 The multiscale framework used in this study depicting the coupled links from the whole continuum knee model to the macro and cell level descriptions

under mechanical stimulation. Peak cartilage strains were used to activate NF-κB pathway, leading to induction of proinflammatory genes

This remodeling approach accounted for both bone growth and bone shape evolution enhancing the ZCC undulating profile and tidemark irregularity. This pattern resembles the finger-like structures that are reported to form during the progression of osteoarthritis (Zizak et al., 2003). The peak strain is also 15–20 % higher in the ACLD knee at the ZCC interface with higher strain closer to the ZCC interface compared to the normal knee. The increase in cartilage strains increased the production of inflammatory cytokines. The findings in this study may explain why altered or traumatic subchondral bone loadings can initiate a degenerative cycle in the cartilage matrix.

2.10 Conclusions

The modeling framework presented in this chapter demonstrates a collection of techniques that can be used to aid patient-specific analysis using computational methods.

This chapter primarily demonstrates efforts towards efficient methods of building subject-specific geometries. However, accurate boundary conditions and material properties are necessary before results can be used with confidence. Patient derived geometries are paramount for both bone and soft tissue when informing clinical decisions. Accurate descriptions of bone provide correct anatomical surface topology and articular features. This is especially important for diseased states like cerebral palsy, which differ significantly from the healthy condition, or when informing implant design for patient surgery. Furthermore, predicting joint contact areas requires accurate models of joint articulations. The anatomical axis is also influenced by the curvature of bone shaft, which in turn allows for accurate moment arm predictions and more meaningful muscle force estimates. Improved soft tissue profiles are important for volume prediction of muscle, which is used to estimate cross-sectional area and hence predict the power generation capacity. Finally, advances in multiscale modeling are being driven by increasing availability of information at all spatial scales. The methods presented here ensure that organ level models are more subject orientated when informing meso and micro descriptions.

Acknowledgements The authors would like to thank all members, past and present, of the Auckland Bioengineering Institute (ABI) musculoskeletal group who have contributed to the presented works, especially, Dr. Katja Oberhofer for her work with host mesh fitting of muscles and Dr. Iain Anderson for his work with patient-specific modeling of hips. This chapter was written with the financial assistance of an Aotearoa bioengineering fellowship awarded to J. Fernandez, a Wishbone Trust grant awarded to V. Shim and a FRST grant awarded to K. Mithraratne and P. Hunter (UOAX0712 and UOAX1006).

References

Ackerman MJ (1998) The visible human project. Proc IEEE 86(3):504–511

Anderson J (1995) Computational fluid dynamics—the basics with applications. McGraw-Hill, New York

Bradley CP, Pullan AJ, Hunter PJ (1997) Geometric modeling of the human torso using cubic Hermite elements. Ann Biomed Eng 25(1):96–111

Dai GH, Gertler JP, Kamm RD (1999) The effects of external compression on venous blood flow and tissue deformation in the lower leg. J Biomech Eng 121(6):557–564

Dobrin PB, Littooy FN et al (1988) Mechanical and histological changes in canine vein grafts. J Surg Res 44:259–265

Downie SP et al (2007) Role of MRI in investigating the effects of elastic compression stockings on the deformation of the superficial and deep veins in the lower leg. J Magn Reson Imaging 26(1):80–85

Downie SP et al (2008) Effects of elastic compression stockings on wall shear stress in deep and superficial veins of the calf. Am J Physiol, Heart Circ Physiol 294(5):H2112–H2120

FCAT (Federative Committee on Anatomical Terminology) (2011) Terminologia anatomica. International anatomical terminology, 2nd edn. Thieme, Stuttgart

Fernandez JW et al (2005) A cerebral palsy assessment tool using anatomically based geometries and free-form deformation. Biomech Model Mechanobiol 4(1):39–56

Fernandez JW, Hunter PJ (2005) An anatomically based patient-specific finite element model of patella articulation: towards a diagnostic tool. Biomech Model Mechanobiol 4(1):20–38

Fernandez JW et al (2004) Anatomically based geometric modeling of the musculo-skeletal system and other organs. Biomech Model Mechanobiol 2(3):139–155

Garny A et al (2008) CellML and associated tools and techniques. Philos Trans R Soc, Math Phys Eng Sci 366(1878):3017–3043
Gray H (2008) Gray's anatomy: the anatomical basis of clinical practice, 40th edn. Churchill Livingstone/Elsevier, Edinburgh/Amsterdam
Hill AV (1938) The heat of shortening and the dynamic constants of muscle. Proc R Soc Lond B, Biol Sci 126(843):136–195
Hunter PJ (1995) Myocardial constitutive laws for continuum mechanics models of the heart. Adv Exp Med Biol 382:303–318
Hunter PJ (1995) Myocardial constitutive laws for continuum models of the heart. In: Sideman S, Beyar R (eds) Molecular and subcellular cardiology. Springer, New York, pp 303–318
Hunter PJ (2004) The IUPS physiome project: a framework for computational physiology. Prog Biophys Mol Biol 85(2–3):551–569
Hunter PJ, Borg TK (2003) Integration from proteins to organs: the physiome project. Nat Rev Mol Cell Biol 4(3):237–243
Hunter PJ, McCulloch AD, ter Keurs HE (1998) Modeling the mechanical properties of cardiac muscle. Prog Biophys Mol Biol 69(2–3):289–331
Huxley AF (1957) Muscle structure and theories of contraction. Progress in biophysics & molecular biology, vol 7. 255 pp
Meier P, Blickhan R (2000) In: Herzog W (ed) Skeletal muscle mechanics: from mechanism to function. Wiley, Bognor Regis, pp 207–224
Nam J et al (2009) Biomechanical thresholds regulate inflammation through the NF-kappa B pathway: experiments and modeling. PLoS ONE 4(4):e5262
Narracott AJ et al (2007) Influence of intermittent compression cuff design on calf deformation: computational results. In: 2007 annual international conference of the IEEE Engineering in Medicine and Biology Society, pp 6335–6338
Nash MP, Hunter PJ (2000) Computational mechanics of the heart—from tissue structure to ventricular function. J Elast 61(1–3):113–141
Oberhofer K et al (2009) Anatomically-based musculoskeletal modeling: prediction and validation of muscle deformation during walking. Vis Comput 25(9):843–851
Pivonka P et al (2008) Model structure and control of bone remodeling: a theoretical study. Bone 43(2):249–263
Rivlin RS (1948) Large elastic deformations of isotropic materials. 1. Fundamental concepts. Philos Trans R Soc Lond Ser A, Math Phys Sci 240(822):459–508
Shim VB et al (2007) The use of sparse CT datasets for auto-generating accurate FE models of the femur and pelvis. J Biomech 40(1):26–35
Shim VB et al (2008) Development and validation of patient-specific finite element models of the hemipelvis generated from a sparse CT data set. J Biomech Eng 130(5):051010
Spitzer VM et al (1995) The visible-human (male and female). Radiology, vol 197. 533 pp
Wriggers P, Krstulovic-Opara L, Korelc J (2001) Smooth C-1-interpolations for two-dimensional frictional contact problems. Int J Numer Methods Eng 51(12):1469–1495
Zahalak GI (2000) The two-state cross-bridge model of muscle is an asymptotic limit of multi-state models. J Theor Biol 204(1):67–82
Zizak I et al (2003) Characteristics of mineral particles in the human bone/cartilage interface. J Struct Biol 141(3):208–217

http://www.springer.com/978-94-007-4551-3

Patient-Specific Computational Modeling
Calvo Lopez, B.; Peña, E. (Eds.)
2012, VII, 193 p., Hardcover
ISBN: 978-94-007-4551-3